AIChE
JOURNAL

A machine learning approach for electrical capacitance tomography measurement of gas–solid fluidized beds

Qiang Guo[1,2] | Mao Ye[1] | Wuqiang Yang[3] | Zhongmin Liu[1]

[1]Dalian National Laboratory for Clean Energy and National Engineering Laboratory for MTO, Dalian Institute of Chemical Physics, Chinese Academy of Sciences, Dalian, China

[2]University of Chinese Academy of Sciences, Beijing, China

[3]School of Electrical and Electronic Engineering, The University of Manchester, Manchester, UK

Correspondence
Mao Ye, Dalian National Laboratory for Clean Energy and National Engineering Laboratory for MTO, Dalian Institute of Chemical Physics, Chinese Academy of Sciences, Dalian 116023, China.
Email: maoye@dicp.ac.cn

Abstract

Electrical capacitance tomography has been widely used to obtain key hydrodynamic parameters of gas–solid fluidized beds, which is normally realized by first reconstructing images and then by analyzing these images. This indirect approach is time-consuming and hence difficult for on-line monitoring. Meanwhile, considering recurrence of similar flow patterns in fluidized beds, most of these calculations are repetitive and should be avoided. Here, we develop a machine learning approach to address these problems. First, superficial gas velocity linear-increasing strategy is used to perform high-throughput experiments to collect a large amount of training samples. These samples are used to train the map from normalized capacitance measurements to key parameters that obtained by an iterative image reconstruction algorithm off-line. The trained model can then be used for on-line monitoring. Preliminary tests revealed that the trained models show good prediction and generality for the estimation of the overall solid concentration and the equivalent bubble diameter.

KEYWORDS

electrical capacitance tomography, fluidized bed, high-throughput experiment, machine learning, on-line monitoring

1 | INTRODUCTION

Gas–solid fluidized beds are commonly used in industry, such as coal conversion, power generation, pharmaceutical granulation, and polymerization. Accurate measurement of the hydrodynamic characteristics is of paramount importance to the design, control, and optimization of fluidized beds in these processes. In the past decades, both intrusive and nonintrusive measurement techniques have been developed.[1,2] Normally, intrusive methods provide only single point measurements and tend to disrupt the hydrodynamics in the region of the vicinity of the probe.[3] Nonintrusive methods, such as process tomography, meanwhile, can be used to visualize the entire flow field without causing any disturbance to the flow. Compared to other process tomographic methods, electrical capacitance tomography (ECT) is the most mature and ideal for measurement of gas–solid fluidized beds because of the

Dedicated to the 70th anniversary of Dalian Institute of Chemical Physics, CAS.

advantages of no radiation, high temporal resolution, robustness, withstanding high temperature and high pressure, and low cost.[4–8]

In ECT measurement, a set of electrodes is mounted around the periphery of the fluidized bed under investigation. Because the gas and fluidized particles have different permittivity, once the distribution and/or concentration of the fluidized particles vary, the interelectrode capacitance will change accordingly. These changes in capacitance are measured by the sensing electronics and further used to reconstruct an image, in which each pixel is assigned a gray level to represent the material distribution, that is, the solid concentration, by a specific image reconstruction algorithm.[9–11] By postprocessing the obtained image, some key hydrodynamic parameters, such as the overall solid concentration, bubble position, and bubble size, can then be estimated.[5,8,10] Therefore, key hydrodynamic parameters are obtained in an indirect manner (see later in step 2 of Figure 2).

However, there are two main difficulties associated with ECT image reconstruction.[10–14] First, it is severely under-determined due

to the number of independent capacitance measurements is much less than the number of pixels in an image. Second, the characteristics of soft-field sensing make the reconstructed images sensitive to noise in raw capacitance measurements. To address these problems, many image reconstruction algorithms have been proposed so far and have been reviewed by Yang and Peng[11] and Cui et al.[12] Among all the proposed algorithms, Landweber iteration algorithm is generally accepted to be able to generate high-quality images in most cases.[9-12,15] However, the iterative process of the Landweber iteration algorithm is time-consuming and hence not suitable for on-line measurement. In addition, it is laborious to carry out postprocessing of the reconstructed images to obtain key hydrodynamic parameters because additional computing time is needed. Therefore, it is essential to develop an alternative approach for on-line monitoring of key hydrodynamic parameters for flow regime identification, fluidization quality characterization, feedback control, and fault detection of gas–solid fluidized beds by the use of ECT.

Note that although the two-phase flow in gas–solid fluidized beds exhibits very complex chaotic behavior,[16,17] many researches indicated recurrence of similar flow patterns.[6,18] In this regard, most of the expensive calculations needed for the material distribution reconstruction and postprocessing are repetitive and can be possibly avoided via a universal data-driven key parameter prediction recipe.

Recent years have seen that machine learning is making a big impact in chemical engineering. Novel applications include heterogeneous catalyst design,[19] crystal identification,[20] automated optimization for continuous flow chemistry,[21] and multiphase flow pattern recognition.[22] Some attempts were also made to extend the application of machine learning to ECT measurements with respect to key parameter prediction without recourse to tomographic images. Mohamad-Saleh and Hoyle[23] used artificial neural networks to directly estimate key parameters for characterizing gas–water flows from normalized capacitance measurements. Zainal-Mokhtar and Mohamad-Saleh[24] trained a multilayer perceptron artificial neural network and used it to estimate the oil fraction in a pipeline with various ECT sensor parameters. Wang and Zhang[25] used a model trained by support vector machine to identify flow regime of gas–oil flows. These works apparently indicated that machine learning may be used to realize on-line measurement for key parameter estimation without image reconstruction. However, the limitations of the above works are that they focused only on some simple distributions with stationary objects by numerical simulations but not on practical problems such as gas–solid fluidized beds. A possible reason is the lack of training samples from a suitable experimental facility.

The aim of this work is to apply machine learning to ECT without image reconstruction for on-line measurement of key hydrodynamic parameters in real gas–solid fluidized beds. To efficiently collect a large amount of sample data that traverse many possible flow patterns in a short time period, we proposed a high-throughput experimental strategy with linearly increasing the superficial gas velocity (u_g) in the fluidized bed. Two key hydrodynamic parameters, that is, the overall solid concentration and the equivalent bubble diameter, were considered in this work. Based on the two measured parameters, we further

studied the flow regime transition from fixed bed to bubbling bed via the solid-like and fluid-like states[26] and the evolution of the bubble size in bubbling fluidized beds for Geldart A particles to illustrate the effectiveness of this machine learning approach.

The organization of this article is as follows. First, experimental setup, experimental methods, and ECT image reconstruction and postprocessing are briefly described. Then, a flowchart of the proposed machine learning approach is given. Next, the performance and generality of the trained model to predict the overall solid concentration are evaluated and discussed. Afterwards, some results regarding the prediction of the equivalent bubble diameter are given, followed by a short summary of the power and limitations of the machine learning approach. Finally, the paper ends with some conclusions.

2 | EXPERIMENTAL SETUP AND DATA PROCESSING

2.1 | Experimental setup

Figure 1a shows the experimental setup used in the overall solid concentration prediction research, which was adapted from our recent work.[26] Three cylindrical fluidized beds with different inner diameters, 30, 50, and 70 mm, were designed. The associated wall thickness of these fluidized beds was also different, say 2.2, 2.5, and 2.9 mm for the 30, 50, and 70-mm fluidized beds, respectively (see Figure 1a). All these fluidized beds were made of quartz glass and had a height of 1 m. Airflow under ambient conditions was introduced to the bottom of the fluidized beds through distributors made of expanded polystyrene foams with the average pore size of 10 μm. The flow rate of air was precisely controlled by a Brooks mass flow controller (Brooks SLA5800 Series). The structure of ECT sensors used for the three fluidized beds was similar, as shown in Figure 1b, with eight measurement electrodes stuck onto the outside wall of the quartz tube and covered by an earthed screen to eliminate external interference. The vertical height of the electrodes was 25 mm, and the electrodes covered 90% of the whole area. As shown in Figure 1a, the mid-position of the ECT sensors was located at 262.5 mm above the distributor. Therefore, the measured region encompassed a height between 250 and 275 mm above the distributor.

Two fluid catalytic cracking (FCC) powders (FCC I and FCC II) and an Al_2O_3 powder (Al_2O_3 I), were used as bed materials. Their particle size distributions and main physical properties are shown in Figure 1c and Table 1, respectively. According to Geldart's classification,[27] these fluidized particles all belong to typical Geldart A particles (see Supporting Information Figure S1).

The ECT sensor needs to be calibrated before measurement. This was done by first emptying the measured fluidized bed and then recording the interelectrode capacitance as C_L. Next, a known quantity of a specified powder was poured into the bed, and the bed was tapped to make the particles closely packed. The interelectrode capacitance at this state was measured as C_H. Such calibration makes the interelectrode capacitance for all flow patterns lie within the range between C_L and C_H. After calibration, u_g was set to a sufficiently large
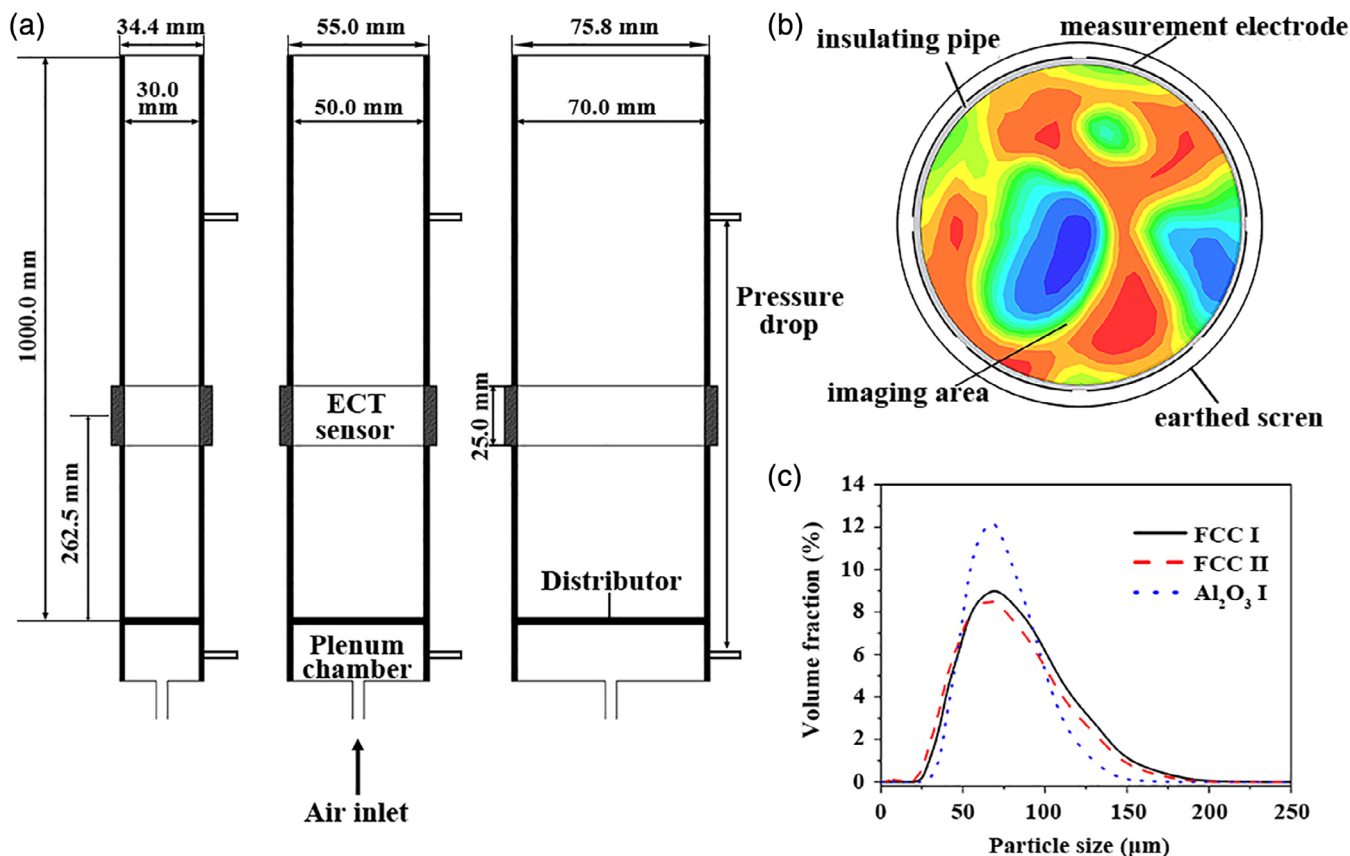
FIGURE 1 (a) Experimental setup, (b) 8-electrode ECT sensor structure, and (c) particle size distribution of the fluidized powders used in the overall solid concentration prediction research

value to make the bed vigorously fluidized in the bubbling regime. Then, u_g was slowly decreased to zero, letting the bed be loosely packed (the packed bed height was about 380 mm for all experiments), which was regarded as the initial bed state in further fluidization process.

A dual-electrode excitation strategy was used for measurement, that is to say, two adjacent electrodes were used as excitation electrodes in turn and the other electrodes as detection electrodes. In this way, the total number of independent capacitance measurements was 48 for the 8-electrode ECT sensor. An AC-based ECT system with a signal-to-noise ratio of 73 dB[28] was used for capacitance measurement.

For comparison, the bed pressure drop and its fluctuation were also measured by using a differential pressure transducer. More specifically, the positive and negative sides of the transducer were connected to taps below the distributor and at the top end of the freeboard, respectively. The pressure drop across the distributor was first determined as a function of u_g with the tube being empty. Then, the bed pressure drop was obtained by subtracting the distributor pressure drop from the measured total pressure drop.

2.2 | Experimental methods

To collect a large amount of sample data for training, a high-throughput experimental strategy was proposed by linearly increasing u_g in the fluidized bed. During a linear-increasing stage, u_g was programmed to

increase linearly from 0 to 11.5 mm/s in a relatively short time period. Different durations, say 180, 300, 600, 900, 1,800, 3,600, and 7,200 s, were used. Supporting Information Figure S2a shows the change in u_g in each duration. Note that as the response time of the used flow controller was about 1 s, the increase in u_g was not strictly linear, instead a small step with the length of about 1 s was observed (see Supporting Information Figure S2b). The data acquisition rate of the used ECT system was 60 frames per second. Therefore, the numbers of samples for different durations were 10,800, 18,000, 36,000, 54,000, 108,000, 216,000, and 432,000, respectively. In this way, a large amount of sample data that traverse many flow patterns can be collected. These collected data, after processing, were stored as training samples for machine learning.

For comparison, u_g step-increasing experiments were also carried out. In this case, a sufficiently long duration, say 15 min, was remained at each u_g to ensure that the bed can reach a dynamic equilibrium, and then the measurement results were recorded in a 100 s time period, resulting in 6,000 and 12,000 measurements for ECT and pressure fluctuation, respectively.

2.3 | Image reconstruction and postprocessing

To show the material distribution, the ECT sensing area was divided into 64×64 pixels, resulting in 3,228 effective pixels in the circular

TABLE 1 Physical properties of the fluidized powders

Powder	Density (ρ_p, kg/m^3)[a]	Mean particle diameter (d_p, μm)[b]	Fines content (F_{45}, %)[c]	Relative permittivity[d]
FCC I	1,300	69.5	16.4	2.22
FCC II	1,260	66.3	22.5	2.13
Al$_2$O$_3$ I	1,950	71.2	9.5	2.49
Al$_2$O$_3$ II	1,950	98.6	3.5	2.51
MTO	1,450	89.6	5.8	3.18
Glass beads	2,300	92.0	2.1	3.42

[a]The density of particles ρ_p was measured by water displacement technique.
[b]The mean particle diameter d_p was calculated as the Sauter mean diameter.
[c]The fines content F_{45} is the fraction of fines with the size less than 45 μm.
[d]The relative permittivity was estimated from the average of all the opposite electrode pairs in an ECT sensor with internal electrodes at closely packed bed state.

imaging region. The projected Landweber iteration algorithm, which can generate satisfactory images in most cases,[9–12,15] was used. The formula of this algorithm is written as

$$g_k = P\left(g_{k-1} + \alpha_k S^T \left(\lambda - S g_{k-1}\right)\right) \tag{1}$$

$$P[f(x)] = \begin{cases} 0 & \text{if } f(x) < 0 \\ f(x) & \text{if } 0 \le f(x) \le 1 \\ 1 & \text{if } f(x) > 1 \end{cases} \tag{2}$$

where g is the gray level of image pixels, S is the normalized sensitivity matrix, and k is the index of iteration steps. The projection operator P is used to constrain the reconstructed image to ensure $g \in [0,1]$. To improve the convergence speed, the step length α is changed during iteration as defined by[29]

$$\alpha_k = \frac{\left\| S^T (\lambda - S g_{k-1}) \right\|}{\left\| SS^T (\lambda - S g_{k-1}) \right\|} \tag{3}$$

The initial image of the Landweber iteration algorithm g_0 is obtained by the linear back projection method,[11] which is the simplest single-step algorithm for ECT, as given by

$$g_0 = \frac{S^T \lambda}{S^T u_\lambda} \tag{4}$$

where u_λ is a unity vector. A drawback of the Landweber iteration algorithm is its semiconvergence characteristic. Therefore, the image quality is not always improved with the increase in the number of iterations, which makes it difficult to determine the number of iterations in advance. Usually, a predefined threshold indicating the distance between two successive reconstructed images is used to mark the stop of the iteration.[15] However, the optimal threshold

is flow pattern dependent. We have tested different thresholds and found that on average, a value of 0.01 can give the best estimation of key hydrodynamic parameters (the overall solid concentration and the equivalent bubble diameter) in our cases. Therefore, the iteration of the Landweber iteration algorithm stops following Equation 5.

$$\| g_k - g_{k-1} \| \le 0.01 \tag{5}$$

The parameter λ in Equations 1, 3, and 4 is the normalized capacitance vector calculated by

$$\lambda = \frac{C_M - C_L}{C_H - C_L} \tag{6}$$

where C_M is the measured capacitance vector for an arbitrary distribution, and C_L and C_H are the capacitance vectors recorded during system calibration.

The sensitivity matrix can be calculated by numerical simulation of potential distributions based on quasi-static field assumption and then by dot multiplying two potential distributions.[30,31]

$$S_{ij}^*(x,y) = -\iint_{p(x,y)} \frac{\nabla \varphi_i(x,y)}{V_i} \cdot \frac{\nabla \varphi_j(x,y)}{V_j} \, dxdy \tag{7}$$

where S_{ij}^* defines the sensitivity between the ith and jth electrodes at the location of the pixel $p(x,y)$, and $\varphi_i(x,y)$ and $\varphi_j(x,y)$ are the potential distributions inside the imaging domain when the ith and jth electrodes are excited by applying voltages of V_i and V_j, respectively.

Then, S^* is normalized as

$$S_{mn} = \frac{S_{mn}^*}{\sum_{n=1}^{N} S_{mn}^*} \tag{8}$$

where S_{mn} and S_{mn}^* are the entries in the mth row and nth column of S and S^*, respectively.

Supporting Information Figure S3 shows the normalized sensitivity distribution averaged over all electrode pairs for ECT sensors used in the three fluidized beds. Some quantitative data such as the maximum, minimum, and standard deviation (SD) of the sensitivity shown in Supporting Information Figure S3 are summarized in Supporting Information Table S1. As can be seen, the sensitivity matrix changes with the dimension of ECT sensors.

With the reconstructed material distribution, key hydrodynamic parameters can be obtained by postprocessing. For example, the overall solid concentration can be obtained by pixel averaging:

$$\beta = \theta \cdot \bar{g} = \theta \cdot \frac{\sum_{i=1}^{N} g_i s_i}{\sum_{i=1}^{N} s_i} \tag{9}$$

where θ is the solid concentration of the packed bed, s is the area of each image pixel, and N is the total number of pixels in the image.

The accuracy of the Landweber iteration algorithm to estimate some key hydrodynamic parameters in gas–solid fluidized beds has been evaluated by several studies.[9,10,32,33] The results showed that the relative error lies within ±5% for the overall solid concentration[9,10,32,33] and ± 15% for the equivalent bubble diameter.[9,10,32] This confirms that the Landweber iteration algorithm can be used to obtain the overall solid concentration and the equivalent bubble diameter with acceptable accuracy.

3 | FLOWCHART OF THE MACHINE LEARNING APPROACH

In this work, machine learning is applied to on-line measurement of key hydrodynamic parameters in real gas–solid fluidized beds by using ECT but without image reconstruction. Figure 2 shows the flowchart of the machine learning approach. At first, u_g linear-increasing strategy, originally used by Ye et al.[34] in discrete particle model simulations, is used to perform high-throughput experiments to collect a large amount of training samples that traverse many possible flow patterns in a short time period. Then at the second step, key hydrodynamic parameters in the training samples are calculated by postprocessing the material distribution reconstructed by the Landweber iteration algorithm off-line. Next, supervised machine learning is used to train the map from the normalized capacitance measurements to the calculated key hydrodynamic parameters on the training samples. With the trained model, key hydrodynamic parameters can be directly predicted from the measured interelectrode capacitance. Therefore, on-line monitoring can be achieved. Note that in model training and further prediction, the model input can be either all the normalized interelectrode capacitance or their principal components, and the output is the concerned key hydrodynamic parameter calculated based on postprocessing the image reconstructed by the Landweber iteration algorithm. The proposed machine learning approach can be used to predict any key hydrodynamic parameters in gas–solid fluidized beds. In this work, the overall solid concentration and the equivalent bubble diameter were considered.

4 | PREDICTION OF THE OVERALL SOLID CONCENTRATION

4.1 | Comparison of different machine learning models

From the viewpoint of statistics, predicting the overall solid concentration from the measured capacitance is a regression problem. Therefore, all machine learning models suitable for regression problems can be used. To assess the performance of different machine learning models, four popular models, that is, linear regression, regression tree, support vector machine regression, and feedforward network regression, were used to train on samples collected in u_g linear-increasing experiments in 3,600 s for FCC I powder fluidized in the 50-mm fluidized bed. The trained models were then validated against the data from u_g linear-increasing experiments in 1,800 s for the same powder and fluidized bed. A brief introduction of the used models and training details to prevent overfitting are provided in Supporting Information.

Figures 3 and 4 show the correlation plots between the overall solid concentration obtained based on postprocessing the reconstructed material distribution and predicted by different machine learning models when all 48 normalized capacitance measurements and their 4 principal components (see Supporting Information Figure S4) are used as the model inputs, respectively. For a quantitative comparison, Supporting Information Figure S6 shows the root mean square error for different models and different inputs. It can be seen that for the regression tree model, there are always some scattered points along the 45° line irrespective of the input, where the maximum error can be as large as 0.04, and many points lie outside the ±1% error line. While for other three machine learning models, most of the predicted points lie within the ±1% error line, showing good prediction performance. It is also noted that except for the regression tree model, all models give better results when all 48 measurements are used as model input (also see Supporting Information Figure S6). This can be easily understood from the measurement strategy of ECT, in which gas–solid flow on a cross section is scanned by an array of measurement electrodes from different viewing angles. Therefore, all 48 interelectrode capacitance measurements contribute to the
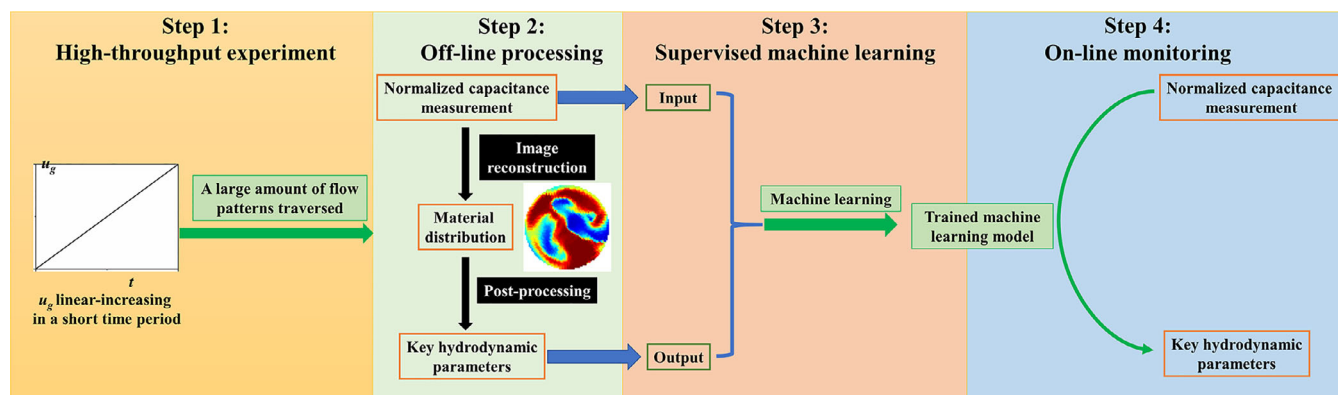

FIGURE 2 Flowchart of the proposed machine learning approach for the measurement of gas–solid fluidized beds using ECT

estimation of the overall solid concentration. The unusual performance of the regression tree model may be associated with the structure of the trained tree.[35]

Overall, the feedforward network regression model with all 48 measurements as input gives the best prediction results. However, when the input is changed to four principal components, the performance worsens significantly. For the simplest linear regression model, the prediction results are satisfied no matter what kind of input is used. Considering both the prediction performance and model complexity, the linear regression model with four principal components as input was chosen finally.

Note that using principal components as model input is not necessarily superior to that with all 48 interelectrode capacitance measurements as input in terms of computational cost in model training and further prediction. This is because the scale of data in the problems discussed in this work is still small (see Supporting Information Table S2). Principal component analysis is normally favorable for situations where a significantly large amount of data is required as training input. However, considering the potential extension of current machine learning approach to wide applications of on-line process tomography, in which the scale of data as training samples might be substantially enlarged, the model with four principal components as input was still chosen in this work.

4.2 | Comparison of different size of training samples

It is well known that fluidization behavior of Geldart A particles is quite different from other particles, because a unique feature characterized by Geldart A particles is that there is an interval of nonbubbling expansion regime, which is also called homogeneous fluidization or particulate fluidization, between the minimum fluidization velocity (u_{mf}) and minimum bubbling velocity (u_{mb}).[27,36] Recently, by using ECT, camera recording, and pressure fluctuation measurements, we experimentally verified that during the homogeneous expansion regime, both solid-like and fluid-like states exist,[26] which indicate that the stability of homogeneous fluidization for Geldart A particles may have two distinct origins: in the solid-like homogeneous fluidization regime, interparticle forces dominate; while in the uniform nonbubbling fluid-like fluidization regime, fluid dynamics dominate. Supported by camera recording and pressure fluctuation measurements, it was found that the profile of the SD of the overall solid concentration obtained by ECT against u_g (see Supporting Information Figure S7 for FCC I powder fluidized in the 50-mm fluidized bed. Note that the average and SD were calculated from the time series of the 6,000 overall solid concentration measurements at each u_g in u_g step-increasing experiments) provides a robust and reliable way to distinguish different fluidization regimes. Three plateaus with small SD shown in this profile correspond to the fixed bed, solid-like homogeneous fluidization, and uniform nonbubbling fluid-like fluidization regimes, respectively, and a sharp increase in SD marks the transition to the bubbling fluidization regime. The gas velocities at the terminal point of each plateau are u_{mf}, the transition velocity u_c, and u_{mb}, respectively. For the profile of the average of the overall solid concentration against u_g, two turning points with one corresponding to u_{mf} and the other referring to the so-called bed contraction phenomenon for Geldart A particles are shown. Note that the overall solid concentration in our previous work[26] was obtained on the basis of postprocessing the material distribution reconstructed by the Landweber iteration algorithm, which is very time-consuming.

To check if the machine learning approach can also predict the three plateaus, the linear regression was used to train on samples collected in u_g linear-increasing experiments in seven different durations, that is, 180, 300, 600, 900, 1,800, 3,600, and 7,200 s, where different durations correspond to different size of the training samples. These trained seven different linear regression models were then used to predict the fluctuation of the overall solid concentration on data collected in u_g step-increasing experiments.
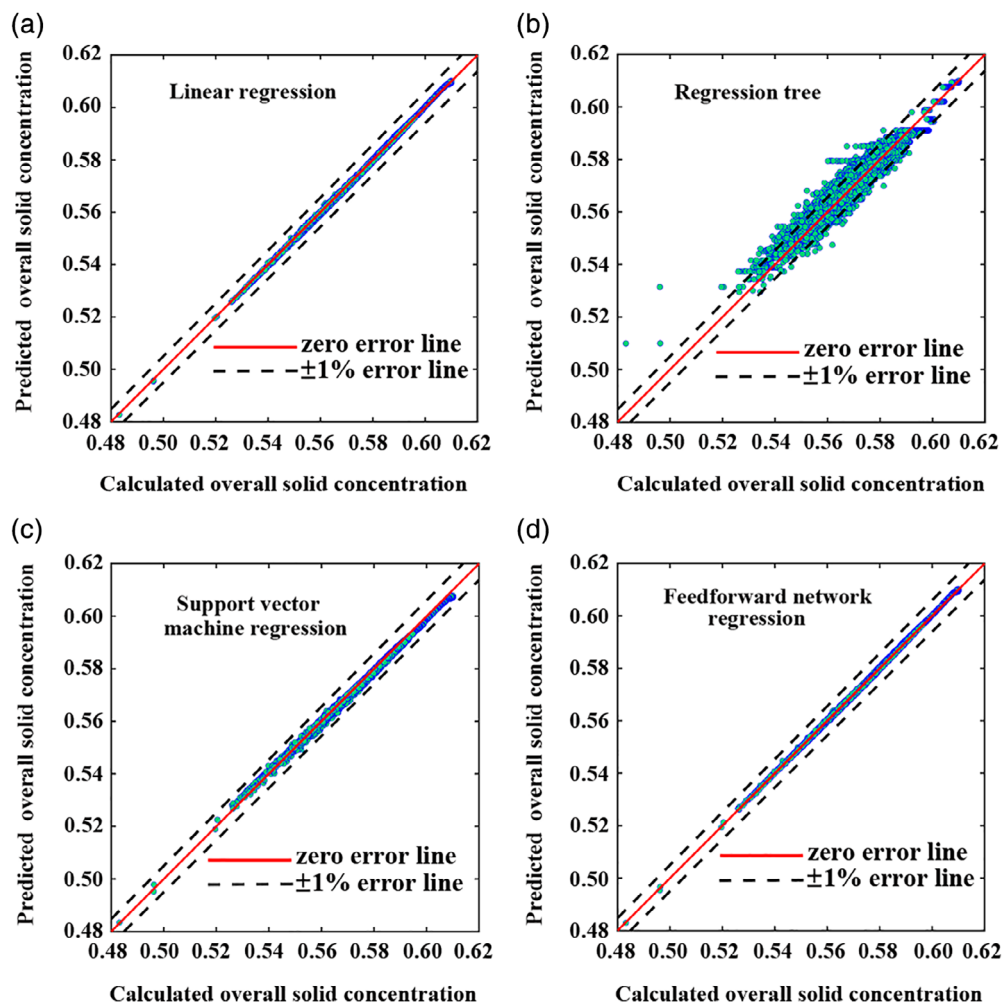
Figure 5 shows the profiles of the average and SD of the predicted overall solid concentration against u_g, alongside those calculated by postprocessing for FCC I powder fluidized in the 50-mm fluidized bed. Clearly, the profile of the average of the overall solid concentration against u_g predicted by all the trained models coincides well with that calculated by postprocessing. In addition, two turning points also agree well for different models. But for the profile of the SD of the overall solid concentration against u_g, only the models trained using samples collected in 3,600 and 7,200 s can well predict the three plateaus. For other models trained on samples collected in shorter time, the SD of the overall solid concentration in the fixed bed regime are overpredicted to the values close to those in the solid-like homogeneous fluidization regime, which make these two plateaus level off as a plateau. Therefore, these models cannot distinguish between the fixed bed and solid-like homogeneous fluidization regimes.

In u_g linear-increasing experiments, the fluctuation of the raw interelectrode capacitance arises from the combination of the change in gas flow rate and fluctuation of gas–solid flow patterns. When u_g linearly increases in a relatively short duration, the change in gas flow rate becomes significant and thus dominates over the small fluctuation of gas–solid flow patterns in the fixed bed regime. The trained model learns well this situation. From this point of view, it is not surprising that the SD of the overall solid concentration in the fixed bed regime predicted by the models trained on the samples collected in a relatively short duration (less than 3,600 s) is larger. In other fluidization regimes, the effect of the fluctuation of gas–solid flow patterns dominates over the change in gas flow rate. Therefore, the SD of the overall solid concentration predicted by the trained models agree well with those by postprocessing regardless of the duration for sample collection. In the following, the linear regression model trained on samples collected in u_g linear-increasing experiments in 3,600 s will be used to evaluate the generality of the trained model.

4.3 | Generality of the trained model

A good machine learning model not only works well for the system similar to that the model was trained on but also provides satisfactory results for systems that the model has not seen before.[13,19,20,35] To further test the generality of the trained model, the data from u_g

FIGURE 3 The overall solid concentration obtained in u_g linear-increasing experiments in 1,800 s for FCC I powder fluidized in the 50-mm fluidized bed. X axis: The results directly from postprocessing. Y axis: The results predicted by the different machine learning models trained on samples collected in u_g linear-increasing experiments in 3,600 s for FCC I powder fluidized in the 50-mm fluidized bed. The model input is all 48 normalized capacitance measurements

step-increasing experiments for different powders as well as different fluidized beds were used as testing samples. Note that the tested model was trained on samples collected in u_g linear-increasing experiments in 3,600 s for FCC I powder fluidized in the 50-mm fluidized bed.

Firstly, the overall solid concentration in the same fluidized bed with two different powders, that is, FCC II and Al$_2$O$_3$ I powders, whose permittivity is different from that of FCC I powder (see Table 1), was predicted. Figure 6 shows the average and *SD* of the overall solid concentration predicted by the trained model alongside those calculated by postprocessing for these two powders. As can be seen, for both powders, the profiles obtained by the machine learning model and postprocessing coincide well with each other, showing that the prediction is very promising.

Secondly, the overall solid concentration in the fluidized beds with different diameters (i.e., 30 and 70 mm) for FCC II powder was predicted. Similar to Figure 6, Figure 7a,b shows the results for FCC II powder fluidized in the two fluidized beds, respectively. As mentioned before, the sensitivity matrix for ECT sensors equipped on fluidized beds will change when the fluidized bed size changes. Even so, the machine learning model originally trained on the 50-mm fluidized bed can also be used to predict the profiles of the 30- and 70-mm fluidized beds, as shown in Figure 7. For a more intuitive presentation,

Figure 8a,b shows the fluctuation of the overall solid concentration at a representative u_g for the 30- and 70-mm fluidized beds, respectively. Clearly, the fluctuation of the overall solid concentration can always be captured by the machine learning model.

To summarize the results presented in Figures 6–8, the machine learning model trained on a specified powder and specified fluidized bed has good generality for other systems with different powders and/or fluidized bed sizes. The reasons for such good generality may be twofold. On the one hand, the input of the machine learning model is obtained from the normalized interelectrode capacitance. With the normalization, the effects of the wall thickness and sensor size on the model input can be minimized.[37] Therefore, for a specified flow pattern, the normalized interelectrode capacitance is similar for different fluidized beds. In turn, the similar interelectrode capacitance obtained from different fluidized beds corresponds to similar flow pattern. On the other hand, the similar flow patterns shared by the fluidized particles grouped in the same category of Geldart's classification are independent on the permittivity of powder and size of fluidized bed (when the change is small).[27] In the investigated range of u_g, the flow behavior transits from the fixed bed to the solid-like homogeneous fluidization regime, then to the uniform nonbubbling fluid-like fluidization regime, and finally to the bubbling fluidization regime for all the studied powders. All these flow behaviors have been traversed in u_g linear-
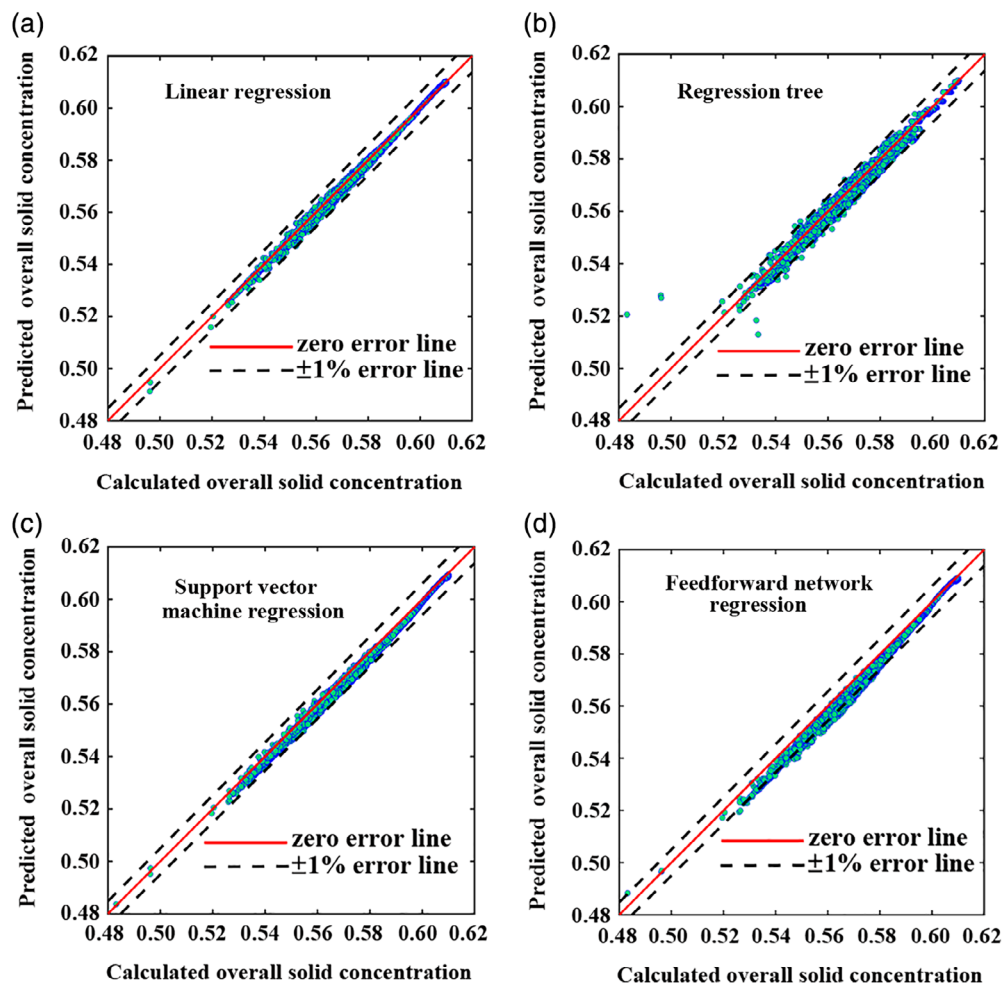
FIGURE 4 The overall solid concentration obtained in u_g linear-increasing experiments in 1,800 s for FCC I powder fluidized in the 50-mm fluidized bed. X axis: The results directly from postprocessing. Y axis: The results predicted by the different machine learning models trained on samples collected in u_g linear-increasing experiments in 3,600 s for FCC I powder fluidized in the 50-mm fluidized bed. The model input is the four principal components of the normalized capacitance measurements

increasing experiments. Therefore, the map from the normalized capacitance measurements to the overall solid concentration corresponding to these flow patterns has been well learned by the trained model, and thus the model has a good generality as shown in this work. It should be stressed that, however, the sizes of the used fluidized beds, say 30, 50, and 70 mm, are relatively small, which make it easy to produce similar flow patterns in these fluidized beds. For a fluidized bed of larger size, the flow patterns may change,[38] and therefore the generality needs to be further checked.

4.4 | Effect of bed size on the transition velocities

In our previous work, only the 50-mm fluidized bed was used to experimentally verify the existence of the solid-like and fluid-like states in the homogeneous expansion regime for Geldart A particles.[26] In this work, three fluidized beds of different sizes were used, which allow to investigate the effect of bed size on the transition velocities. Table 2 lists the transition velocities including u_{mf}, u_c, and u_{mb} for FCC II powder fluidized in different fluidized beds. These transition velocities were identified from the terminal points of the three plateaus in the profile of the SD of the overall solid concentration against u_g, as shown in Figures 7a 6a and 7b for the 30-, 50-, and 70-mm fluidized beds, respectively. Note that the identified transition velocities from

the profile of the SD of the overall solid concentration are in-line with visual observations. In addition, the obtained u_{mf} and u_{mb} correspond well with those from pressure fluctuation measurements. Figure 9a,b show the bed pressure drop normalized by particle weight per unit cross-sectional area (Δp_n) and SD of the bed pressure drop for FCC II powder fluidized in different fluidized beds, respectively. As can be seen, u_{mf} identified from the point where the bed pressure drop across the bed becomes sufficient to balance the particle weight[34,39] (see Figure 9a) and u_{mb} from the point, after which the SD of the bed pressure drop increases sharply[26,40] (see Figure 9b), are the same as the u_{mf} and u_{mb} listed in Table 2 from ECT measurements, respectively. To further quantitatively compare the obtained transition velocities, u_{mf} and u_{mb} calculated from the empirical correlations of Abrahamsen and Geldart[41] are also included in Table 2. Note that the correlations for both u_{mf} and u_{mb} ignore the effect of bed size.

Liu et al.[42] conducted a series of experiments to evaluate the bed size effects on u_{mf} and u_{mb} for different powders and found that both u_{mf} and u_{mb} increase with decreasing bed diameter. Similar conclusions were draw by Rao et al.[43] for u_{mf} and Shaul et al.[44] for u_{mb}. u_c, as a new transition velocity demarcating the solid-like homogeneous fluidization and uniform nonbubbling fluid-like fluidization regimes, have many common features with u_{mf}, as both indicating the bed changing from a stationary state to a suddenly dynamic state.[26] Therefore, it is

reasonable to speculate that the trend of u_c with bed size follows u_{mf}. In our work, it can be concluded from Table 2 that the three transition velocities for FCC II powder in the 30- and 50-mm fluidized beds are similar, while when the bed size further increases to 70 mm, both u_{mf} and u_c become smaller and u_{mb} becomes larger.

For gas–solid fluidization, an interesting and well-documented phenomenon is that a pressure overshoot over the particle weight per unit cross-sectional area occurs when u_g reaches u_{mf}, and a qualitative inference is that the stronger the wall friction and/or interparticle cohesive forces, the higher the overshoot, and vice versa.[34,45,46] As shown in Figure 9a, the pressure overshoot for the 30- and 50-mm fluidized beds is similar and larger than that for the 70-mm fluidized bed, indicating the synergistic effect of wall friction and interparticle cohesive forces is at the similar order for the 30- and 50-mm fluidized beds and larger than that for the 70-mm fluidized bed. This may partially explain why the transition velocities of the 30- and 50-mm fluidized beds are similar and u_{mf} and u_c of the two beds are larger than that of the 70-mm fluidized bed. However, the increase in u_{mb} in the 70-mm fluidized bed seems inconsistent with the previous conclusion.[42,44] It is noted that some points in Figure 5 by Liu et al.[42] and Figure 4 by Shaul et al.[44] also show an increase in u_{mb} when the bed size increases. We argued that, therefore, the different trend of u_{mb} with increase in bed diameter may need further investigation. A possible tentative explanation is that the effect of bed size on u_{mb} is two-fold. On the one hand, a smaller bed size results in an enhanced wall friction, which delays the u_{mb}. On the other hand, the bed voidage increases with the decrease in bed size,[47] and finally the voidage in a smaller bed is easier to form a bubble. Therefore, the u_{mb} may be a result of the compromise between these two effects. In fact, identification of u_{mb} is a nontrivial task and many controversies exist in literature. For example, some researchers suggested replacing u_{mb}, which is a single velocity, by a velocity range.[48] Nevertheless, as stressed before, the transition velocities listed in Table 2 are unified for ECT, visual observations, and pressure fluctuation measurements, and the obtained u_{mf} and u_{mb} in three beds are all close to those calculated from the empirical correlations of Abrahamsen and Geldart.[41]

5 | PREDICTION OF THE EQUIVALENT BUBBLE DIAMETER

The proposed machine learning approach can be used to predict any key hydrodynamic parameters in gas–solid fluidized beds, such as the overall solid concentration, bubble position, and bubble size using the same procedure as shown in Figure 2 with little modification. To further confirm this, the proposed approach was used to predict bubble parameters including the equivalent diameter, centroid coordinate, major axis length, and minor axis length of a bubble in bubbling fluidized beds in a parallel work. Here, some preliminary results regarding the equivalent bubble diameter are shown.

Figure 10a shows the experimental setup used in the bubble parameter prediction research, in which two cylindrical fluidized beds (FB1 and FB2) available in our laboratory were used. FB1 was made of
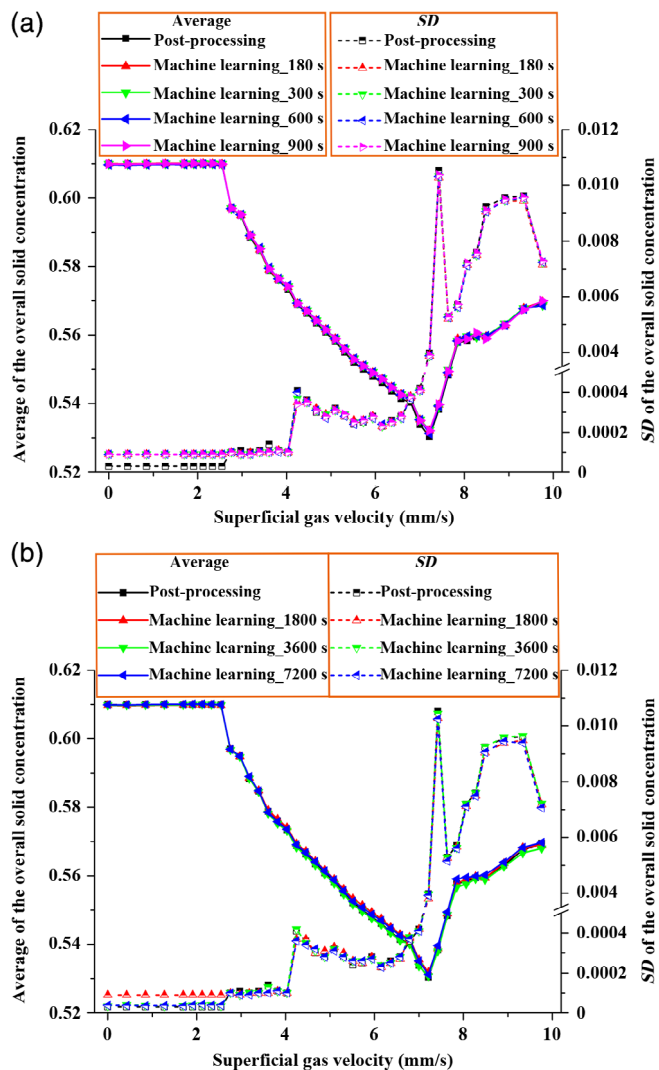

FIGURE 5 Average and *SD* of the overall solid concentration against u_g in u_g step-increasing experiments for FCC I powder fluidized in the 50-mm fluidized bed. The overall solid concentration here is obtained by postprocessing and predicted by the linear regression models trained on samples collected in u_g linear-increasing experiments in (a) 180, 300, 600, and 900 s and (b) 1,800, 3,600, and 7,200 s for FCC I powder fluidized in the 50-mm fluidized bed

quartz glass, while FB2 was made of Perspex. Airflow under ambient conditions was distributed to the beds through an expanded polystyrene foam for FB1 and a sintered steel porous plate for FB2. The dimensions of the two beds are shown in Figure 10a, in which FB1 had an inner diameter of 60 mm and an outer diameter of 66 mm, while FB2 had an inner diameter of 80 mm and an outer diameter of 89 mm. An FCC powder (FCC II) was fluidized in FB1, while an Al_2O_3 powder (Al_2O_3 II), a methanol to olefins (MTO) powder, and a glass bead powder were fluidized in FB2. Figure 10c shows their particle size distributions, and Table 1 summarizes their main physical properties. All these fluidized powders belong to Geldart A particles (see Supporting Information Figure S1). Different from the ECT sensors used in the overall solid concentration research, the ECT sensors used here had twelve measurement electrodes, as shown in Figure 10b. The vertical height of
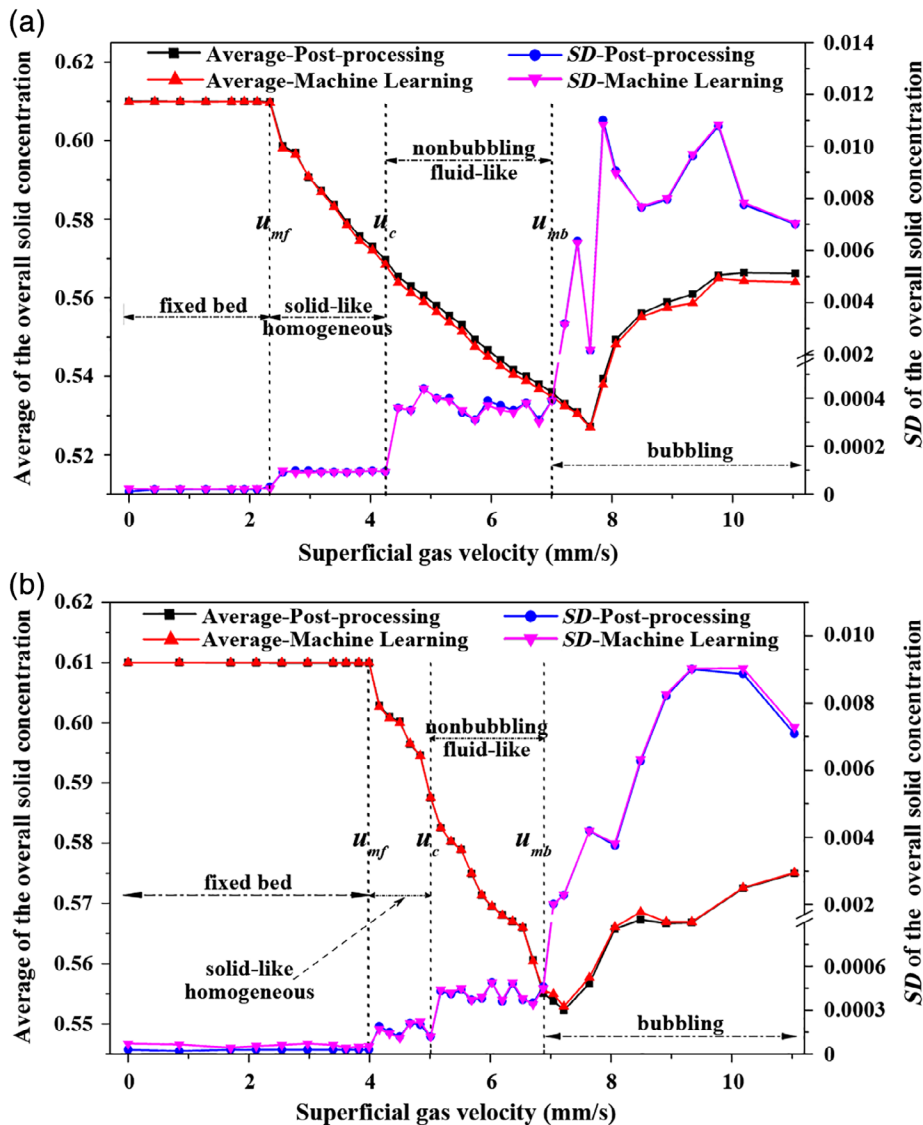
(a)

(b)

FIGURE 6 Average and SD of the overall solid concentration against u_g in u_g step-increasing experiments for (a) FCC II powder and (b) Al_2O_3 I powder fluidized in the 50-mm fluidized bed. The overall solid concentration here is obtained by postprocessing and predicted by the linear regression model trained on samples collected in u_g linear-increasing experiments in 3,600 s for FCC I powder fluidized in the 50-mm fluidized bed

the electrodes of FB1 and FB2 were 30 and 40 mm, respectively. The mid-position of the ECT sensor of FB1 and FB2 was located at 200 and 365 mm above the distributor, respectively.

Following the flowchart shown in Figure 2, u_g linear-increasing strategy was used to perform high-throughput experiments to collect a large amount of bubble data in a relatively short time period. More specifically, u_g was programmed to increase linearly from 0 to 145.2 mm/s for FB1 and 0 to 182.4 mm/s for FB2 in a duration of 3,600 s. These data, after processing, were stored as training samples to perform supervised machine learning for the prediction of the equivalent bubble diameter. The prediction consists of two steps, which require two machine learning models, as shown in Figure 11a. The first model is a classification machine that is used to judge from the normalized capacitance measurements whether bubbles are formed on the cross section of the measured region. The output of the classification machine has two labels indicating the absence or presence of bubbles, respectively. When the output of the classification machine is *absence*, the equivalent bubble diameter is directly given a value of 0. While when the output of the classification machine is *presence*, the second model begins to work to predict from

the normalized capacitance measurements the equivalent diameter of the formed bubbles, which is a regression problem. Here, a bubble was defined as the continuous region with the solid concentration reconstructed by the Landweber iteration algorithm lower than a predefined threshold. The diameter of a bubble was defined as the diameter of a circular bubble with equivalent cross-sectional area, and the equivalent bubble diameter was obtained as the number-averaged bubble diameter. In literature, the threshold used to distinguish the boundary between the bubble and emulsion phases ranges from 0.15 to 0.3 and a threshold of 0.25 was used in this work. Due to the studied fluidized beds had small bed diameters and were operated with a large initial aspect ratio, it was observed in experiments that in most cases, only a single bubble could pass through the ECT measurement region at a time.

For the 12-electrode ECT sensor, a total of 120 independent capacitance measurements can be obtained with a dual-electrode excitation strategy. The principal component analysis shows that the former 12 components can retain more than 98% variance for the training samples collected in u_g linear-increasing experiments in

FIGURE 7 Average and *SD* of the overall solid concentration against u_g in u_g step-increasing experiments for FCC II powder fluidized in (a) the 30-mm fluidized bed and (b) the 70-mm fluidized bed. The overall solid concentration here is obtained by postprocessing and predicted by the linear regression model trained on samples collected in u_g linear-increasing experiments in 3,600 s for FCC I powder fluidized in the 50-mm fluidized bed
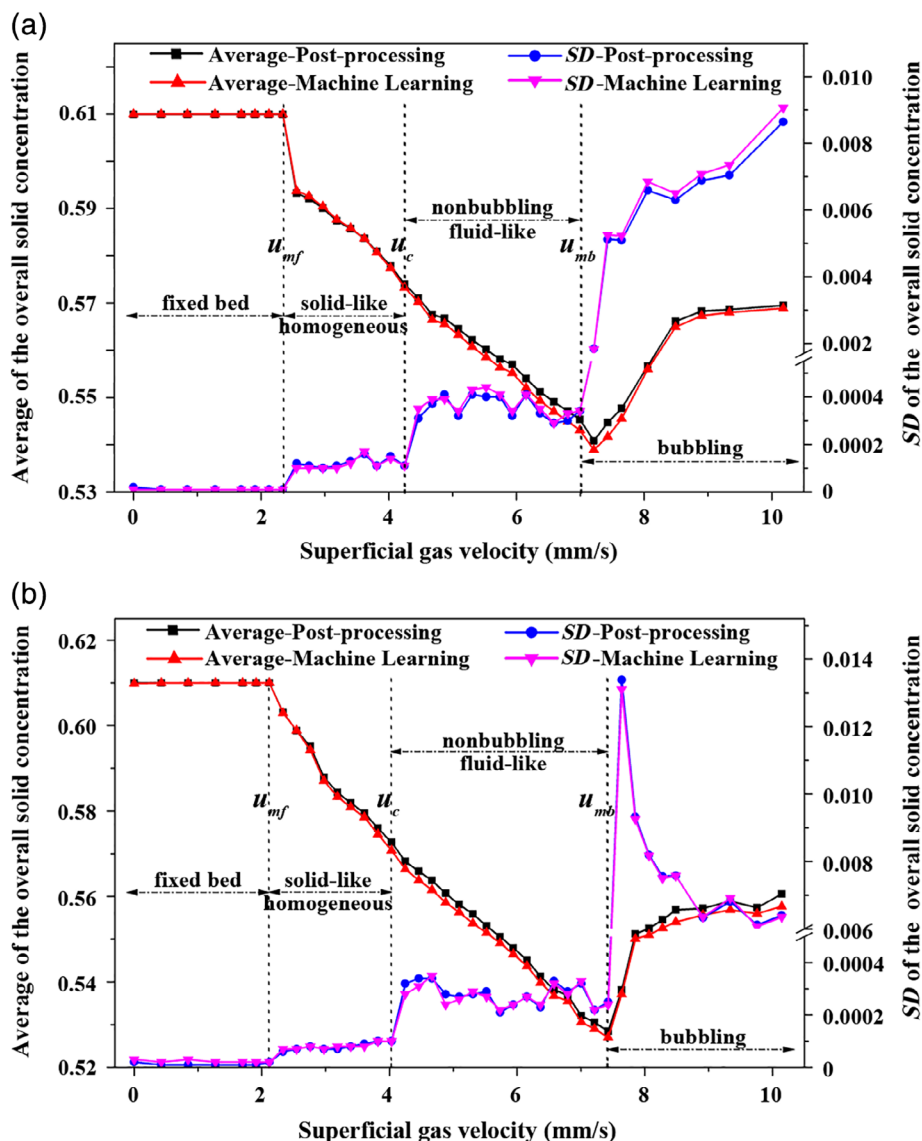
3,600 s for Al_2O_3 II powder fluidized in FB2. Therefore, these converted 12 principal components were used as the model input.

In addition to function fitting, neural networks are also good at classification.[49] Therefore, feedforward network was used for both classification and regression machines for the prediction of the equivalent bubble diameter. Figure 11b,c shows, respectively, their structures. A total of 25 neurons were included in the hidden layer for both machines. For the classification machine, a tan-sigmoid transfer function and a softmax transfer function were used in the hidden layer and in the output layer, respectively. While for the regression machine, except for the number of neurons in the hidden layer, other settings were the same as that in the prediction of the overall solid concentration (see Supporting Information).

Both the classification and regression machines were trained on samples collected in u_g linear-increasing experiments in 3,600 s for Al_2O_3 II powder fluidized in FB2. Note that all data were used to train the classification machine, while only the data indicating the presence of bubbles were selected to train the regression machine.

Table 3 summarizes the accuracy of the trained classification machine for the prediction of the presence of bubbles within the data collected in u_g linear-increasing experiments for different powders fluidized in FB1 and FB2. As can be seen, the trained classification machine shows high accuracy. For the same powder and same fluidized bed as those used for training, the accuracy can be as high as 99.5%. For particles or fluidized beds other than those used for training, the accuracy can still be higher than 96%, indicating a good generality.

Figure 12 further shows the correlation plots between the equivalent bubble diameter obtained based on postprocessing the material distribution and predicted by the trained machine learning models for different powders fluidized in FB1 and FB2. It is clear that due to some measurements are classified wrongly by the trained classification machine, say the machine predicts the absence of bubbles for a measurement that has bubbles, or vice versa, some points fall on the X axis and Y axis, showing large deviation. Except for these points, the rest predicted by the machine learning models lie within an acceptable error margin of those obtained via postprocessing. The relative error
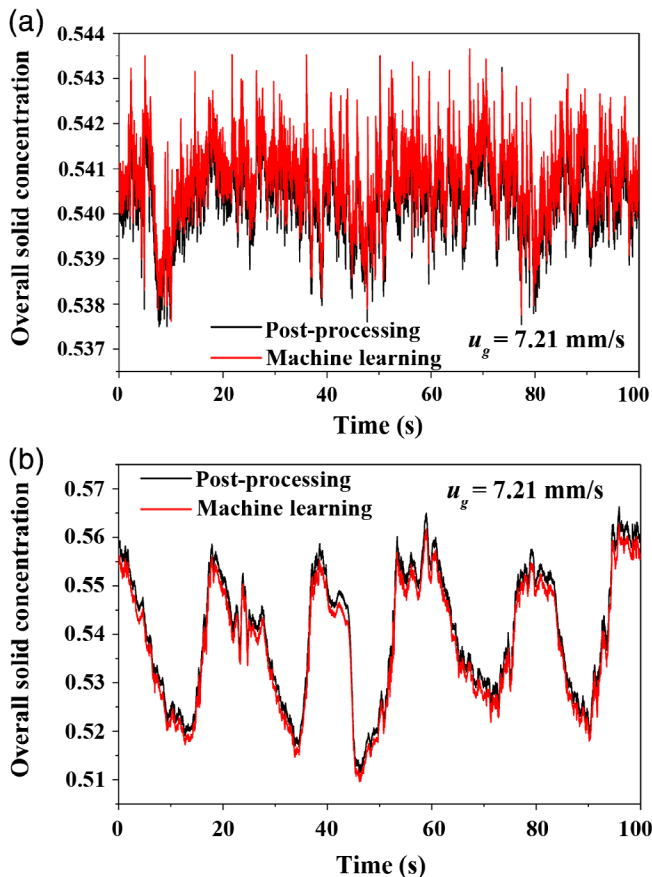
FIGURE 8 Fluctuation of the overall solid concentration at a representative u_g in u_g step-increasing experiments for FCC II powder fluidized in (a) the 30-mm fluidized bed and (b) the 70-mm fluidized bed. The overall solid concentration here is obtained by postprocessing and predicted by the linear regression model trained on samples collected in u_g linear-increasing experiments in 3,600 s for FCC I powder fluidized in the 50-mm fluidized bed
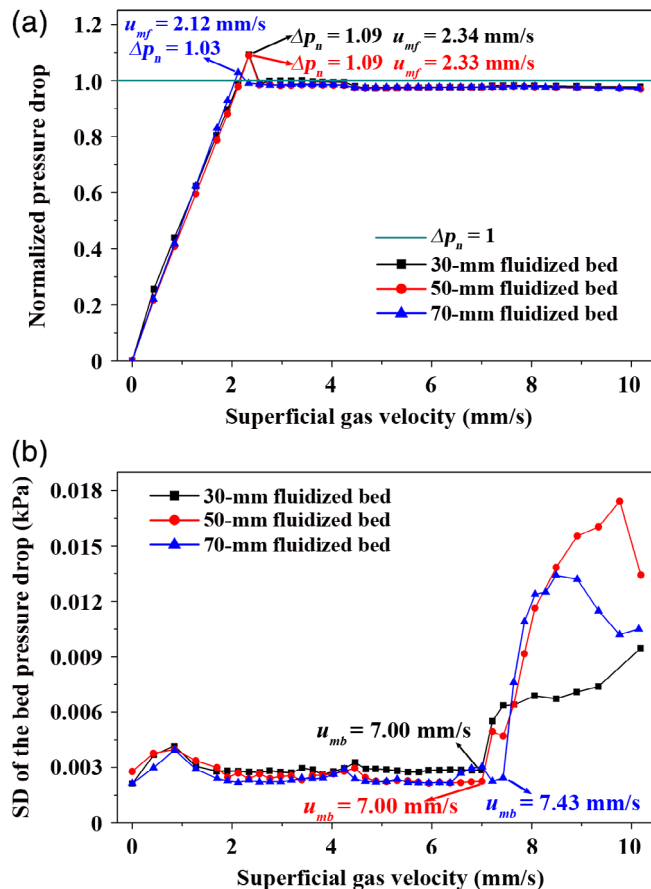

FIGURE 9 (a) Bed pressure drop normalized by particle weight per unit cross-sectional area and (b) SD of the bed pressure drop against u_g in u_g step-increasing experiments for FCC II powder fluidized in different fluidized beds

for Al_2O_3 II powder fluidized in FB2, which are the same as those used for training, is within ±10% (see Figure 12a). If different powders, that is, MTO catalyst (see Figure 12b) and glass beads (see Figure 12c), were fluidized in the same fluidized bed (i.e., FB2), most of the relative error is within ±10%. Even when both the powders and fluidized beds were changed to those that the trained machine learning models have not seen before, the relative error is still within ±20% (see Figure 12d).

The trained machine learning models were also used to predict the evolution of the equivalent bubble diameter against u_g in u_g step-increasing experiments, as shown in Figure 13. The characteristic

equivalent bubble diameter at each u_g was obtained as follows. First, the time series of the equivalent bubble diameter at each u_g was divided into 50 segments. Then, the maximum diameter in each segment was detected. Finally, the average of the 50 maximum equivalent bubble diameters was chosen. The error bars in Figure 13 were calculated as the SD of the 50 maximum equivalent bubble diameters. As a reference, the estimated bubble diameters from the established empirical correlations of Rowe,[50] Werther,[51] Mori and Wen,[52] and Yacono[53] are shown alongside the experimental size in Figure 13. Clearly, independent of the powder and fluidized bed, the predicted bubble diameter and the associated error bar agree well with those obtained via postprocessing and lie within the window of the established correlations. For a more intuitive

TABLE 2 Transition velocities of FCC II powder in different fluidized beds

Bed size, mm	u_{mf}, mm/s[a]	u_c, mm/s[a]	u_{mb}, mm/s[a]	$u_{mf,c}$, mm/s[b]	$u_{mb,c}$, mm/s[b]
30	2.34	4.25	7.00	2.30	7.07
50	2.33	4.24	7.00	2.30	7.07
70	2.12	4.03	7.43	2.30	7.07

[a]u_{mf}, u_c, and u_{mb} were identified from the profile of the SD of the overall solid concentration, which are in-line with visual observations. Furthermore, u_{mf} and u_{mb} correspond well with those from pressure fluctuation measurements.
[b]u_{mf} and u_{mb} with the subscript c mean the values calculated from the empirical correlations of Abrahamsen and Geldart.

FIGURE 10 (a) Experimental setup, (b) 12-electrode ECT sensor structure, and (c) particle size distribution of the fluidized powders used in the bubble parameter prediction research
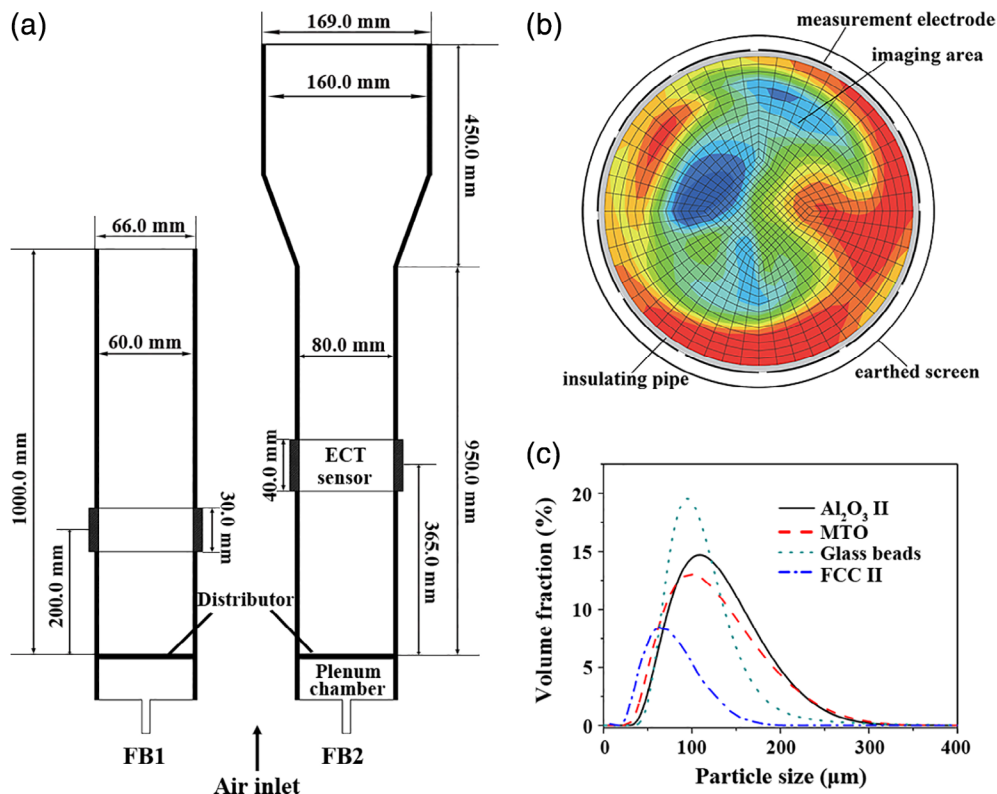
presentation, similar to Figure 8, Figure 14 shows the fluctuation of the equivalent bubble diameter at a representative u_g for different powders and fluidized beds. As can be seen, the general fluctuation trend of the equivalent bubble diameter can be well captured by the trained machine learning models.

Comparing the prediction results for the equivalent bubble diameter to the overall solid concentration (for example, comparing between Figures 12 and 4), it is noted that even though more complex neural network model was used, the predication results for the equivalent bubble diameter are not as excellent as those for the overall solid concentration. This reflects the common knowledge that measurement of the equivalent bubble diameter is much more difficult than that of the overall solid concentration[4,9,10] and may be associated with the different properties of the two parameters, in which the overall solid concentration is a global quantity averaged over the whole bed cross section, while the equivalent bubble diameter is closely related to local material
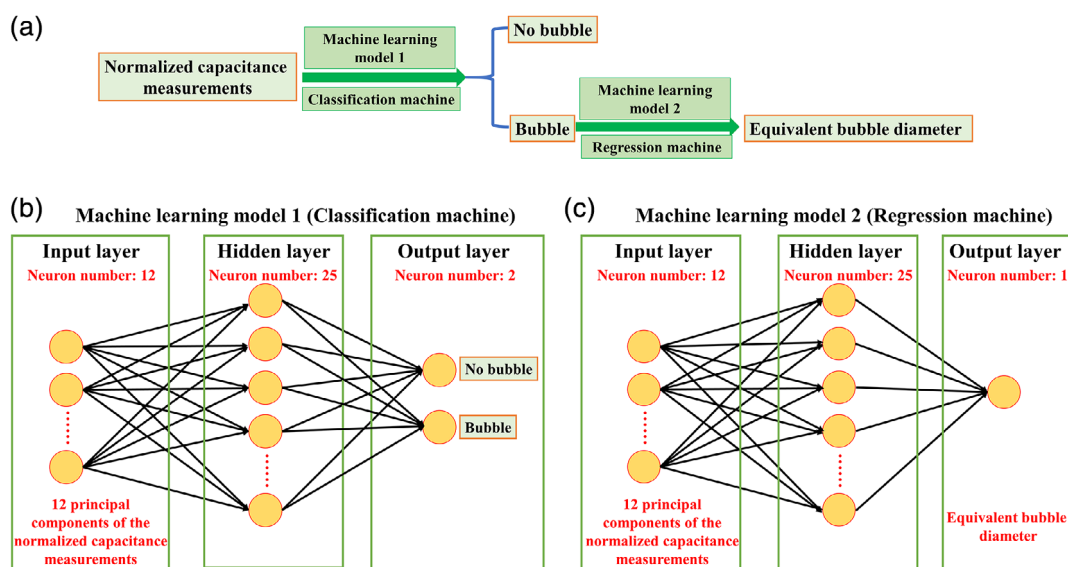

FIGURE 11 (a) Steps for the prediction of the equivalent bubble diameter, (b) feedforward network structure of the classification machine, and (c) feedforward network structure of the regression machine

TABLE 3 Accuracy of the trained classification machine for the prediction of the presence of bubbles within the data collected in u_g linear-increasing experiments for different powders and fluidized beds

Fluidized bed	Fluidized powder	Accuracy (%)
FB2	Al_2O_3 II	99.5
FB2	MTO	97.6
FB2	Glass beads	98.3
FB1	FCC II	96.8

distribution. In addition, when the fluidized bed size is not the same as that used for training, it can be seen from Figures 7 and 8 that the prediction results for the overall solid concentration are still pretty good. While for the equivalent bubble diameter, the prediction results worsen significantly, as shown in Figures 12 and 14. This is because that the overall solid concentration is a dimensionless quantity that is irrelevant to the bed size, while the equivalent bubble diameter may be scaled by the bed size in different fluidized beds. Anyway, the results here still support that the machine learning approach can provide direct estimation of the equivalent bubble diameter, which is valuable in practice. In a parallel work, the machine learning approach was used to predict more bubble parameters including the equivalent diameter, centroid coordinate, major axis length, and minor axis length of a bubble. With

these parameters, a complete description of a bubble in bubbling fluidized beds can be given. This work is now undergoing.

6 | POWER AND LIMITATIONS OF THE MACHINE LEARNING APPROACH

Compared to the indirect method, in which key hydrodynamic parameters are obtained based on postprocessing the reconstructed image by the Landweber iteration algorithm, the power of the machine learning approach can be summarized as follows.

1. The machine learning approach can approximate closely to the results from the indirect method. For example, the predicted overall solid concentration is very close to that by postprocessing. In addition, the *SD* of the overall solid concentration, which can be used to characterize the fluidization regime transition, can also be well captured by the machine learning approach.
2. The machine learning approach is very fast. The reason is that the machine learning approach skips over the time-consuming image reconstruction and postprocessing steps. The typical time needed for the machine learning approach to predict the overall solid concentration with a trained model is about 1 ms on a PC with an
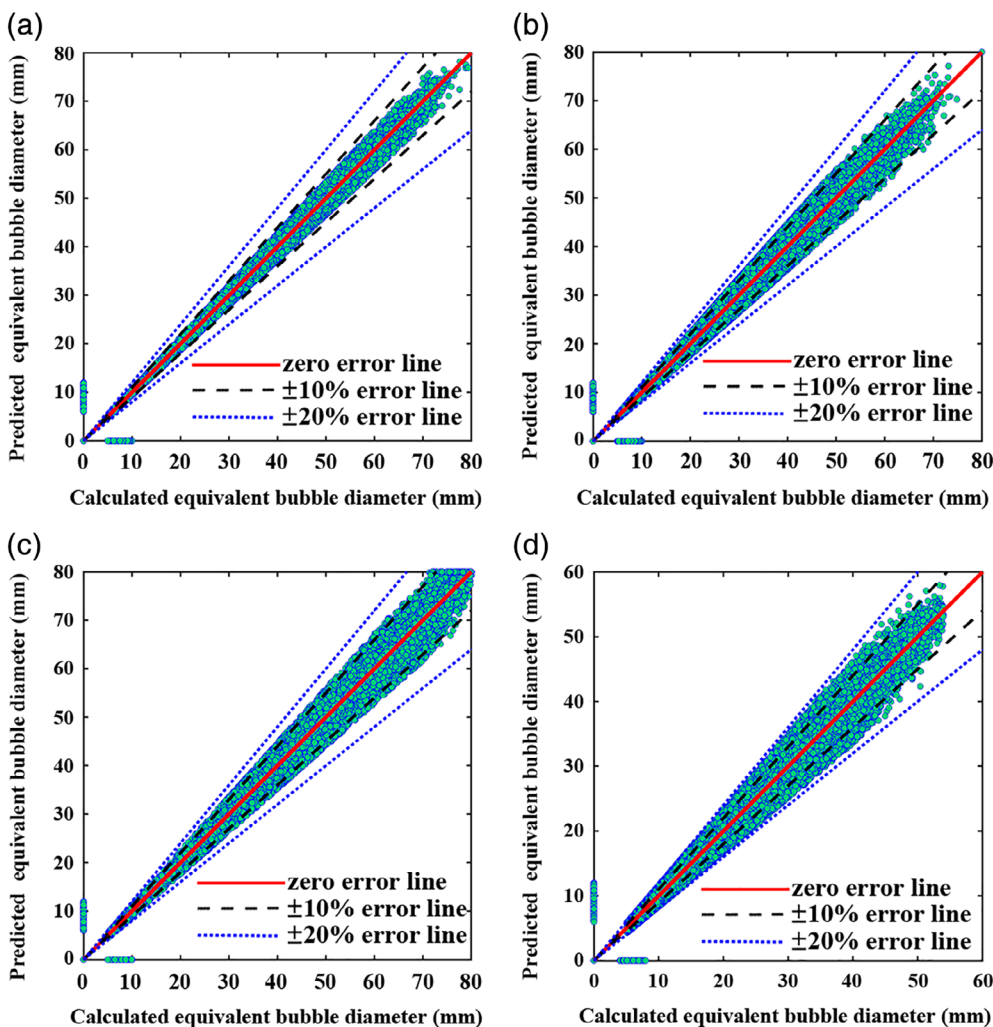

FIGURE 12 The equivalent bubble diameter obtained in u_g linear-increasing experiments in 3,600 s for (a) Al_2O_3 II powder fluidized in FB2, (b) MTO powder fluidized in FB2, (c) glass beads powder fluidized in FB2, and (d) FCC II powder fluidized in FB1. X axis: The results directly from postprocessing. Y axis: The results predicted by the machine learning models trained on samples collected in u_g linear-increasing experiments in 3,600 s for Al_2O_3 II powder fluidized in FB2
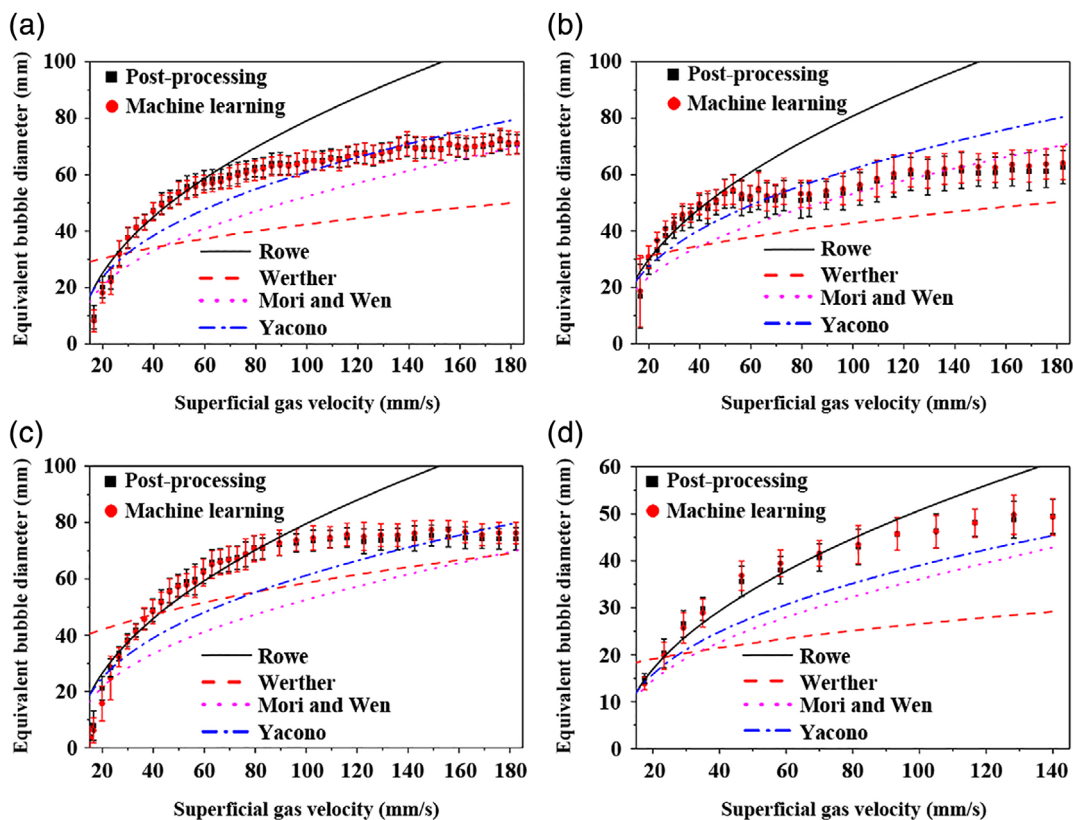
FIGURE 13 Evolution of the equivalent bubble diameter in u_g step-increasing experiments determined by postprocessing, predicted by the machine learning models trained on samples collected in u_g linear-increasing experiments in 3,600 s for Al_2O_3 II powder fluidized in FB2, and calculated by the correlations of Rowe, Werther, Mori and Wen, and Yacono for (a) Al_2O_3 II powder fluidized in FB2, (b) MTO powder fluidized in FB2, (c) glass beads powder fluidized in FB2, and (d) FCC II powder fluidized in FB1

Intel Core i5 3.30 GHz, which is only 0.1% or less of that by the traditional indirect method. Therefore, the machine learning approach has great potential to be used for on-line flow regime identification, fluidization quality characterization, feedback control, and fault detection of gas–solid fluidized beds.

3. The batch processing speed of the machine learning approach is also very fast. The nature of the machine learning approach makes it extremely suitable for batch processing of the data from a large number of measurements. For example, the typical time needed for the machine learning approach to predict the overall solid concentration for 6,000 measurements at each u_g in u_g step-increasing experiments is about 4 s, while the typical time for the traditional indirect method can be as long as tens of minutes.

4. The machine learning approach can be used as a general method in a certain range. The machine learning model trained on a specified powder and fluidized bed can also be used in the measurements of other powders and other fluidized bed sizes if the fluidization patterns do not deviate too much, even though both the permittivity of powders and sensitivity matrix of ECT sensors have been changed.

However, it should be stressed that the output of the training samples is from postprocessing the material distribution reconstructed by the Landweber iteration algorithm, which has certain error when obtaining key hydrodynamic parameters. In this regard, the accuracy

of key hydrodynamics parameters obtained by the machine learning approach in this work can be further improved. This can be done by three potential ways in the future. The first way is to replace the Landweber iteration algorithm with more advanced image reconstruction algorithms, such as those based on total variation.[5,54] The second way is to perform synchronous measurements by ECT with another technique that can obtain key hydrodynamic parameters more accurately. Some direct techniques (i.e., no image reconstruction is needed) like pressure drop measurements and some process tomographic techniques with higher spatial resolution like electron beam X-ray tomography[55] and magnetic resonance imaging technique[56] can be used. The third promising way is to conduct virtual experiments,[10,57] in which true distributions are extracted from the phantoms of CFD simulations and the interelectrode capacitance is calculated from electrostatic simulations. Unfortunately, for the first way, due to the challenging inverse problem of ECT is not avoided, the improvement on the accuracy is limited. In other words, the accuracy obtained by the machine learning approach is still constrained by that from the traditional indirect method. For the latter two ways, both are not realistic at present. A difficulty underlying the second way is making ECT and these mentioned measurement techniques synchronous. Therefore, it may be difficult to construct a one-to-one relationship between the normalized capacitance measurements of ECT and the corresponding key hydrodynamic parameters obtained by other measurement techniques. For the virtual
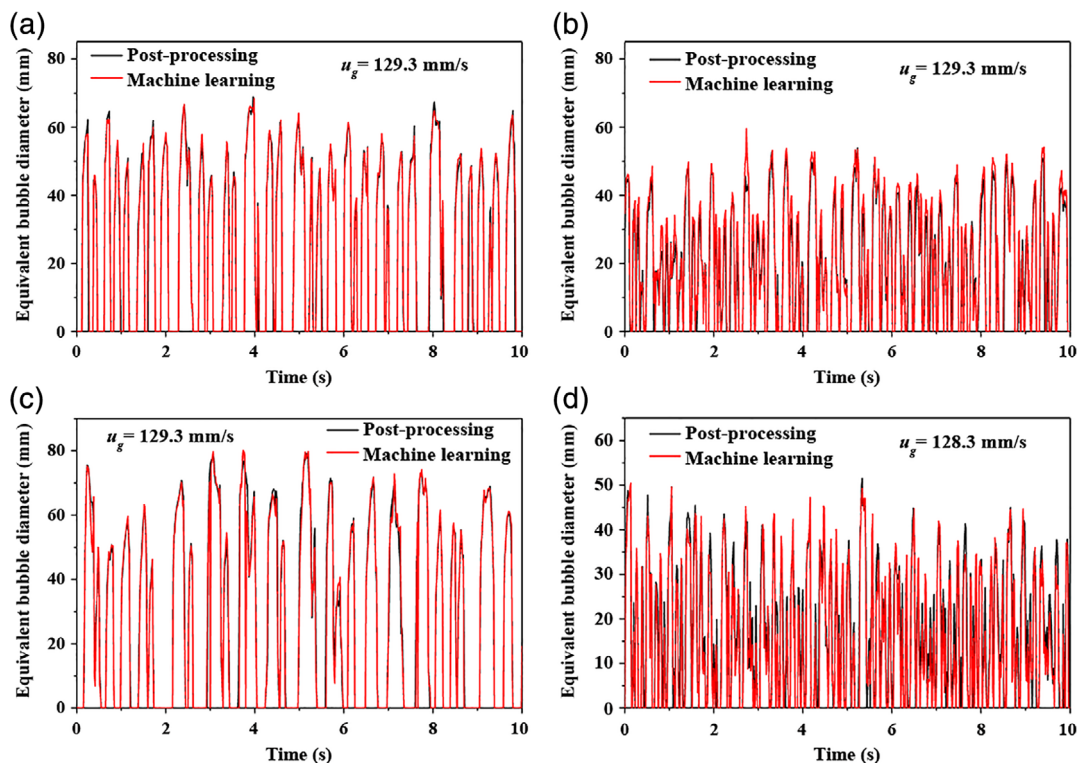
FIGURE 14 Fluctuation of the equivalent bubble diameter at a representative u_g in u_g step-increasing experiments for (a) Al_2O_3 II powder fluidized in FB2, (b) MTO powder fluidized in FB2, (c) glass beads powder fluidized in FB2, and (d) FCC II powder fluidized in FB1. The equivalent bubble diameter here is obtained by postprocessing and predicted by the machine learning models trained on samples collected in u_g linear-increasing experiments in 3,600 s for Al_2O_3 II powder fluidized in FB2

experiments, even though it is attractive because both true key hydrody-namic parameters and the corresponding interelectrode capacitance can be known, the disadvantage is that the state-of-the-art CFD models can-not always predict all flow patterns encountered in a real fluidized bed.[58,59] In addition, the calculated interelectrode capacitance, even though incorporated with the effect of noise, still deviates from the mea-sured data in experiments. In the future, if these problems can be well addressed, the challenging inverse problem of ECT can be truly avoided and key hydrodynamic parameters with higher accuracy can be directly derived from the normalized capacitance measurements by the trained machine learning model. Therefore, any progress in the development of these ways will benefit the machine learning approach proposed in this work.

7 | CONCLUSION

In this work, a general machine learning approach for the measurement of gas–solid fluidized beds using ECT was developed. The method fea-tures that an u_g linear-increasing strategy is used to perform high-throughput experiments to collect a large amount of training samples that traverse different flow patterns and supervised machine learning is used to train the map from the normalized capacitance measurements to key hydrodynamic parameters in the training samples. With the trained model, the time-consuming image reconstruction and

postprocessing steps can be avoided. The goal of on-line monitoring of key hydrodynamic parameters can thus be achieved.

To tentatively show the effectiveness of the proposed machine learning approach, the fluctuation of the overall solid concentration of Geldart A particles in the fixed bed, solid-like homogeneous fluidization, uniform nonbubbling fluid-like fluidization, and bubbling fluidization regimes were concerned in this work. Four machine learning models including linear regression, regression tree, support vector machine regression, and feedforward network regression were used. The perfor-mance of different machine learning models with different model inputs was compared, and the linear regression model with four principal components as model input was chosen. Then, the effect of the size of the training samples on the performance of the trained model to identify different flow regimes was investigated. It was found that a duration of 3,600 s was needed to identify three plateaus in the profile of the *SD* of the overall solid concentration against u_g in u_g step-increasing experiments. Finally, data from different powders and fluidized beds were used to test the generality of the trained model. Due to the normalized form of the model input and the similarity of the fluidization behavior for the same group fluidized particles, a good generality was shown.

The proposed approach was also used to the prediction of the equivalent bubble diameter to show that the approach can be used for any key hydrodynamic parameters with little modification. The prediction of the equivalent bubble diameter requires two trained

machines: a classification machine used for the judgment of the presence of bubbles, and a regression machine used for the prediction of the bubble diameter. Both machines were trained using feedforward network. The results showed that the trained models have good prediction performance and generality.

Although in this work the measurement technique is focused on ECT, the proposed approach can also be applied to other techniques, which are difficult to be used for on-line measurement of gas–solid fluidized beds, such as electron beam X-ray tomography[55] and magnetic resonance imaging technique.[56]

NOTATION

Roman letters

C	capacitance, pF
g	normalized permittivity
S	normalized sensitivity matrix
u_c	transition velocity between the solid-like homogeneous fluidization and uniform nonbubbling fluid-like fluidization regimes, mm/s
u_g	superficial gas velocity, mm/s
u_{mb}	minimum bubbling velocity, mm/s
u_{mf}	minimum fluidization velocity, mm/s
V	potential difference, V

Greek letters

α	step length in the projected Landweber iteration algorithm
β	overall solid concentration
λ	normalized capacitance
u_λ	identity vector (a vector of ones) used in the linear back projection method
θ	packed bed solid concentration
Δp_n	normalized pressure drop

Subscripts

H	high calibration
L	low calibration
M	measurement

Superscripts

$-$	mean value

Abbreviations

ECT	electrical capacitance tomography
CFD	computational fluid dynamics
FCC	fluid catalytic cracking
MTO	methanol to olefins

ORCID

Qiang Guo https://orcid.org/0000-0002-8857-1961
Mao Ye https://orcid.org/0000-0002-7078-2402

REFERENCES

1. van Ommen JR, Mudde RF. Measuring the gas-solids distribution in fluidized beds–a review. *Int J Chem React Eng*. 2008;6: Review R3.
2. Werther J. Measurement techniques in fluidized beds. *Powder Technol*. 1999;102:15-36.
3. Cocco RA, Karri SBR, Knowlton TM, et al. Intrusive probes in riser applications. *AIChE J*. 2017;63:5361-5374.
4. Zhang W, Wang C, Yang W, Wang C-H. Application of electrical capacitance tomography in particulate process measurement–a review. *Adv Powder Technol*. 2014;25:174-188.
5. Chandrasekera TC, Li Y, Moody D, Schnellmann MA, Dennis JS, Holland DJ. Measurement of bubble sizes in fluidised beds using electrical capacitance tomography. *Chem Eng Sci*. 2015;126:679-687.
6. Wang D, Xu M, Marashdeh Q, Straiton B, Tong A, Fan L-S. Electrical capacitance volume tomography for characterization of gas–solid slugging fluidization with Geldart group D particles under high temperatures. *Ind Eng Chem Res*. 2018;57:2687-2697.
7. Huang K, Meng S, Guo Q, et al. High-temperature electrical capacitance tomography for gas–solid fluidised beds. *Meas Sci Technol*. 2018; 29:104002.
8. Weber JM, Mei JS. Bubbling fluidized bed characterization using electrical capacitance volume tomography (ECVT). *Powder Technol*. 2013; 242:40-50.
9. Banaei M, van Sint Annaland M, Kuipers JAM, Deen NG. On the accuracy of Landweber and Tikhonov reconstruction techniques in gas-solid fluidized bed applications. *AIChE J*. 2015;61:4102-4113.
10. Guo Q, Meng S, Wang D, et al. Investigation of gas-solid bubbling fluidized beds using ECT with a modified Tikhonov regularization technique. *AIChE J*. 2018;64:29-41.
11. Yang WQ, Peng L. Image reconstruction algorithms for electrical capacitance tomography. *Meas Sci Technol*. 2003;14:R1-R13.
12. Cui Z, Wang Q, Xue Q, et al. A review on image reconstruction algorithms for electrical capacitance/resistance tomography. *Sens Rev*. 2016;36:429-445.
13. Zheng J, Peng L. An autoencoder-based image reconstruction for electrical capacitance tomography. *IEEE Sens J*. 2018;18:5464-5474.
14. Marashdeh Q, Warsito W, Liang-Shih F, Teixeira FL. Nonlinear forward problem solution for electrical capacitance tomography using feed-forward neural network. *IEEE Sens J*. 2006;6:441-449.
15. Yang WQ, Spink DM, York TA, McCann H. An image-reconstruction algorithm based on Landweber's iteration method for electrical-capacitance tomography. *Meas Sci Technol*. 1999;10:1065-1069.
16. Zhang C, Qian W, Wei F. Instability of uniform fluidization. *Chem Eng Sci*. 2017;173:187-195.
17. Llop MF, Gascons N, Llauró FX. Recurrence plots to characterize gas–solid fluidization regimes. *Int J Multiphase Flow*. 2015;73:43-56.
18. Lichtenegger T, Pirker S. Recurrence CFD–a novel approach to simulate multiphase flows with strongly separated time scales. *Chem Eng Sci*. 2016;153:394-410.

19. Goldsmith BR, Esterhuizen J, Liu J-X, Bartel CJ, Sutton C. Machine learning for heterogeneous catalyst design and discovery. *AIChE J.* 2018;64:2311-2323.

20. Spellings M, Glotzer SC. Machine learning for crystal identification and discovery. *AIChE J.* 2018;64:2198-2206.

21. Schweidtmann AM, Clayton AD, Holmes N, Bradford E, Bourne RA, Lapkin AA. Machine learning meets continuous flow chemistry: automated optimization towards the Pareto front of multiple objectives. *Chem Eng J.* 2018;352:277-282.

22. Ye J, Guo L. Multiphase flow pattern recognition in pipeline–riser system by statistical feature clustering of pressure fluctuations. *Chem Eng Sci.* 2013;102:486-501.

23. Mohamad-Saleh J, Hoyle BS. Determination of multi-component flow process parameters based on electrical capacitance tomography data using artificial neural networks. *Meas Sci Technol.* 2002;13:1815-1821.

24. Zainal-Mokhtar K, Mohamad-Saleh J. An oil fraction neural sensor developed using electrical capacitance tomography sensor data. *Sensors.* 2013;13:11385-11406.

25. Wang HX, Zhang LF. Identification of two-phase flow regimes based on support vector machine and electrical capacitance tomography. *Meas Sci Technol.* 2009;20:114007.

26. Guo Q, Meng S, Zhao Y, et al. Experimental verification of solid-like and fluid-like states in the homogeneous fluidization regime of Geldart A particles. *Ind Eng Chem Res.* 2018;57:2670-2686.

27. Geldart D. Types of gas fluidization. *Powder Technol.* 1973;7:285-292.

28. Yang WQ, York TA. New AC-based capacitance tomography system. *IEE Proc a.* 1999;146:47-53.

29. Liu S, Fu L, Yang WQ. Optimization of an iterative image reconstruction algorithm for electrical capacitance tomography. *Meas Sci Technol.* 1999;10:L37-L39.

30. Process Tomography Ltd. Electrical capacitance tomography system type PTL300E instuction manual. 2005. http://www.tomography.com/pdf/PTL300EV1.pdf.

31. Mou C, Peng L, Yao D, Zhang B, Deyun XA. Calculation method of sensitivity distribution with electrical capacitance tomography. *Chin J Comput Phys.* 2006;23:87-92.

32. McKeen TR, Pugsley TS. The influence of permittivity models on phantom images obtained from electrical capacitance tomography. *Meas Sci Technol.* 2002;13:1822-1830.

33. Pugsley T, Tanfara H, Malcus S, Cui H, Chaouki J, Winters C. Verification of fluidized bed electrical capacitance tomography measurements with a fibre optic probe. *Chem Eng Sci.* 2003;58:3923-3934.

34. Ye M, van der Hoef MA, Kuipers JAM. The effects of particle and gas properties on the fluidization of Geldart A particles. *Chem Eng Sci.* 2005;60:4567-4580.

35. Ahmad MW, Reynolds J, Rezgui Y. Predictive modelling for solar thermal energy systems: a comparison of support vector regression, random forest, extra trees and regression trees. *J Clean Prod.* 2018;203:810-821.

36. Oke O, Lettieri P, Mazzei L. An investigation on the mechanics of homogeneous expansion in gas-fluidized beds. *Chem Eng Sci.* 2015;127:95-105.

37. Ye J, Wang H, Yang W. Characterization of electrical capacitance tomography sensors with different diameter. *IEEE Sens J.* 2014;14:2240-2251.

38. Verma V, Padding JT, Deen NG, Kuipers JAM. Effect of bed size on hydrodynamics in 3-D gas-solid fluidized beds. *AIChE J.* 2015;61:1492-1506.

39. Xie HY, Geldart D. Fluidization of FCC powders in the bubble-free regime: effect of types of gases and temperature. *Powder Technol.* 1995;82:269-277.

40. Rhodes MJ, Wang XS, Nguyen M, Stewart P, Liffman K. Use of discrete element method simulation in studying fluidization characteristics: influence of interparticle force. *Chem Eng Sci.* 2001;56:69-76.

41. Abrahamsen AR, Geldart D. Behaviour of gas-fluidized beds of fine powders part I. Homogeneous expansion. *Powder Technol.* 1980;26:35-46.

42. Liu X, Xu G, Gao S. Micro fluidized beds: wall effect and operability. *Chem Eng J.* 2008;137:302-307.

43. Rao A, Curtis JS, Hancock BC, Wassgren C. The effect of column diameter and bed height on minimum fluidization velocity. *AIChE J.* 2010;56:2304-2311.

44. Shaul S, Rabinovich E, Kalman H. Generalized flow regime diagram of fluidized beds based on the height to bed diameter ratio. *Powder Technol.* 2012;228:264-271.

45. Castellanos A. The relationship between attractive interparticle forces and bulk behaviour in dry and uncharged fine powders. *Adv Phys.* 2005;54:263-376.

46. Galvin JE, Benyahia S. The effect of cohesive forces on the fluidization of aeratable powders. *AIChE J.* 2014;60:473-484.

47. Guo QJ, Xu YQ, Yue XH. Fluidization characteristics in micro-fluidized beds of various inner diameters. *Chem Eng Technol.* 2009;32:1992-1999.

48. Sande PC, Ray S. Fine mesh computational fluid dynamics study on gas-fluidization of Geldart A particles: homogeneous to bubbling bed. *Ind Eng Chem Res.* 2016;55:2623-2633.

49. Tanajura da Silva CE, Filardi VL, Pepe IM, Chaves MA, Santos CMS. Classification of food vegetable oils by fluorimetry and artificial neural networks. *Food Control.* 2015;47:86-91.

50. Rowe PN. Prediction of bubble size in a gas fluidised bed. *Chem Eng Sci.* 1976;31:285-288.

51. Werther J. Effect of gas distributor on the hydrodynamics of gas fluidized beds. *Ger Chem Eng.* 1978;1:166-174.

52. Mori S, Wen CY. Estimation of bubble diameter in gaseous fluidized beds. *AIChE J.* 1975;21:109-115.

53. Yacono CXR. An X-ray Study of Bubbles in Gas Fluidised Bed of Small Particles [Ph.D. Thesis]. London, UK: University of London; 1975.

54. Li K, Chandrasekera TC, Li Y, Holland DJ. A non-linear reweighted Total variation image reconstruction algorithm for electrical capacitance tomography. *IEEE Sens J.* 2018;18:5049-5057.

55. Verma V, Padding JT, Deen NG, et al. Bubble dynamics in a 3-D gas-solid fluidized bed using ultrafast electron beam X-ray tomography and two-fluid model. *AIChE J.* 2014;60:1632-1644.

56. Muller CR, Davidson JF, Dennis JS, et al. Real-time measurement of bubbling phenomena in a three-dimensional gas-fluidized bed using ultrafast magnetic resonance imaging. *Phys Rev Lett.* 2006;96:154504.

57. Meng F, Zhang N, Wang W. Virtual experimentation of beam hardening effect in X-ray CT measurement of multiphase flow. *Powder Technol.* 2009;194:153-157.

58. Gao X, Li T, Sarkar A, Lu L, Rogers WA. Development and validation of an enhanced filtered drag model for simulating gas-solid fluidization of Geldart A particles in all flow regimes. *Chem Eng Sci.* 2018;184:33-51.

59. Lu B, Zhang J, Luo H, et al. Numerical simulation of scale-up effects of methanol-to-olefins fluidized bed reactors. *Chem Eng Sci.* 2017;171:244-255.

SUPPORTING INFORMATION

Additional supporting information may be found online in the Supporting Information section at the end of this article.